Imaging Fracture Zones at Eleven-Mile Canyon Using Anisotropic Least-Squares Reverse-Time Migration

Yunsong Huang[1], Kai Gao[1], Miao Zhang[1], Andrew Sabin[2], and Lianjie Huang[1]

[1] Geophysics Group, Los Alamos National Laboratory, Los Alamos, NM 87545, USA

[2] Navy Geothermal Program Office, China Lake, CA 93555, USA

Keywords

Anisotropic Reverse-time Migration, Eleven-Mile Canyon, Fracture Zone, Geothermal Exploration

ABSTRACT

Accurate imaging of fracture zones is crucial for geothermal energy exploration. Fracture zones and most geologic formations behave as anisotropic media for seismic-wave propagation. Properly accounting for subsurface anisotropic properties is essential for high-resolution imaging of fracture/fault zones for geothermal exploration. We develop a novel anisotropic least-squares reverse-time migration method for reliable imaging of fracture zones. The method employs an efficient implicit wavefield-separation scheme to reduce image artifacts and improve the image quality. We verify the capability of our new imaging method using synthetic data for a geophysical model of the Eleven-Mile Canyon site in Nevada containing several fracture/fault zones. We apply our new method to seismic data acquired along five 2D lines at Eleven-Mile Canyon for geothermal energy exploration. Our imaging results demonstrate that our new anisotropic least-squares reverse-time migration improves image resolution and reduces image artifacts.

1. Introduction

The Eleven-Mile Canyon geothermal exploration site is located near the margins of Dixie Valley, Nevada (Fig. 1, inset). It lies next to the surface rupture terminations of 1954 Fairview Peak – Dixie Valley earthquake sequence (Caskey et al., 1996). In 2013, the U.S. Navy Geothermal Program Office carried out a seismic reflection survey (Alm et al., 2016) along five lines to evaluate the geothermal potential at Eleven-Mile Canyon, NV. Lines 1, 2, 3, and 4 were along west-east direction to cross the valley, while Line 5 lied along north-south direction to intersect Lines 1–3 (Fig. 1). The lines were optimally-oriented perpendicular to the predominant structural fabric of the area to enhance detection horizon/fault detection.
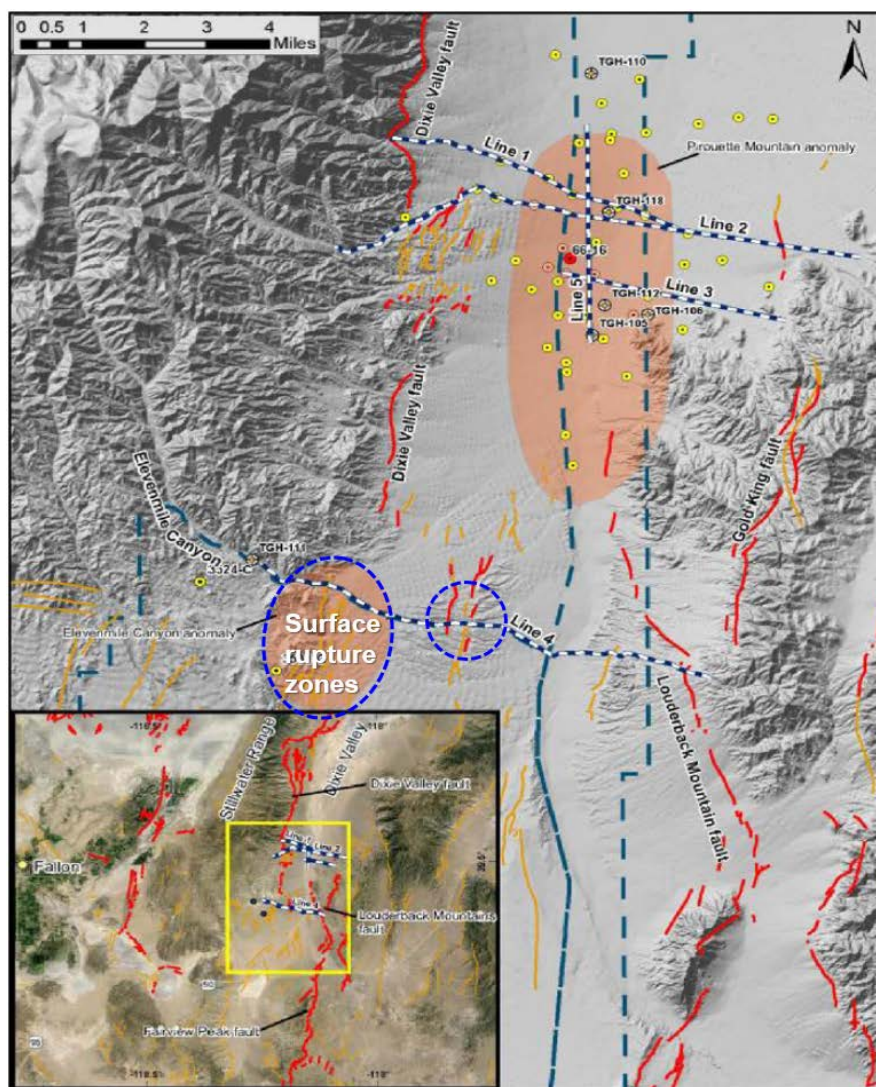
Figure 1: Location map of Eleven-Mile Canyon geothermal exploration site in southern Dixie Valley, Nevada, with five lines of seismic survey depicted in rails. The faults shown are from the U.S. Geological Survey Quaternary fault and fold database. Surface rupture zones correspond to the 1954 earthquake sequence (Unruh et al., 2016).

This geothermal exploration site in Dixie Valley, Nevada, contains a complex network of steeply-dipping faults and fractures, which creates the highly permeable fractures for the production zone at 2-3 kilometers in depth (Unruh et al., 2016). It is important to accurately image and delineate subsurface fracture/fault zones for geothermal exploration and optimizing well placement, because fracture/fault zones may provide paths for hydrothermal flow, but they may also be effective barriers to geothermal flow in some situations (Ba et al., 2015). However, it is particular challenging to accurately image fracture zones because of complex heterogeneities and possible anisotropies in both fracture zones and surrounding rocks.

Reverse-time migration (RTM) is a powerful tool for imaging complex subsurface structures. In essence, RTM relocates the energy in seismic data to subsurface reflectors where the seismic waves are reflected before reaching seismic detectors at the surface for a surface seismic survey. Such a relocation of seismic energy relies on numerical simulations of seismic-wave forward and

backward propagation. When the subsurface media is anisotropic, as is typical in complex geothermal exploration sites (Gao and Huang, 2015), it is crucial to properly account for the subsurface anisotropic properties to allow accurate simulations of seismic wavefields. Anisotropic RTM accounting for anisotropy was recently used for imaging fracture/fault zones at the Eleven-Mile Canyon geothermal exploration site (Zhang et al. 2018).

While RTM performs the aforementioned energy relocation noniteratively, an extension of RTM is termed least-squares RTM (LSRTM) (Nemeth et al., 1999), which iteratively adjusts the subsurface reflectors so that synthetic seismic data would maximally resemble (in the sense of least-squares residue) real seismic data. Because of ambiguity in the velocity model and limited numbers of sources and receivers, the noniterative RTM suffers from migration artifacts. By contrast, because of the feedback control mechanism in the iterative LSRTM, the discrepancy between the imaged reflectors and the physical reflectors is restrained.

In this paper, we apply anisotropic least-squares reverse-time migration to seismic data acquired at the Eleven-Mile Canyon geothermal exploration site for reliable imaging of the fracture/fault zones. First, we validate the effectiveness of our anisotropic LSRTM method using synthetic data for a "typical" anisotropic basin and range geothermal model by comparing the imaging results with those obtained using anisotropic RTM, as well as with those obtained using isotropic LSRTM. Then we apply our anisotropic LSRTM to five 2D lines of surface seismic data acquired at the Eleven-Mile Canyon geothermal exploration site, and compare the images with industrial images and those obtained using anisotropic RTM.

2. Anisotropic Least-Squares Reserve-Time Migration

LSRTM seeks to improve a reflectivity model $\mathbf{m}$ over iterations, by minimizing a least-squares data residue J defined as

$$J = \frac{1}{2} \ \| \mathbf{d}\text{-}\mathbf{Lm} \|^2, \tag{1}$$

where $\mathbf{d}$ represents observed seismic data, and operator $\mathbf{L}$ encapsulates both how seismic wave propagates from sources to reflectors, and how reflected seismic wave propagates to reflectors. To minimize J, $\mathbf{m}$ is updated iteratively, and one algorithm for the iterative update is gradient descent, given as

$$\begin{aligned}
\mathbf{m}^{(k+1)} &= \mathbf{m}^{(k)} - \alpha^{(k)} \nabla_{\mathbf{m}} J \\
&= \mathbf{m}^{(k)} + \alpha^{(k)} \mathbf{L}^T (\mathbf{d}\text{-}\mathbf{Lm}^{(k)}),
\end{aligned} \tag{2}$$

where the superscripts $^{(k)}$ and $^{(k+1)}$ denote the kth and (k+1)[th] iteration, respectively, and $\alpha^{(k)}$ denotes the step length. Note that when $\mathbf{m}^{(k)} = \mathbf{0}$ at the second line of Eq.(2), the line is proportional to $\mathbf{L}^T \mathbf{d}$, which is recognized as the image of RTM. Therefore, RTM is merely the first iteration of LSRTM when starting from $\mathbf{m}^{(0)} = \mathbf{0}$. In general, the term $\mathbf{L}^T(\mathbf{d}\text{-}\mathbf{Lm})$ is the result of an imaging condition, formed by migrating the data residue $(\mathbf{d}\text{-}\mathbf{Lm})$.

In addition, we employ a modified total-variation regularization scheme (Gao et al., 2015). The criterion function in Eq. 1 becomes,

$$J(\mathbf{m},\mathbf{u}) = \min_{\mathbf{m},\mathbf{u}}\{\ \frac{1}{2}\ \|\mathbf{d}\text{-}\mathbf{L}\mathbf{m}\|^2 + \lambda_1 \|\mathbf{m}-\mathbf{u}\|^2 + \lambda_2 \|\mathbf{u}\|_{\mathrm{TV}}\},\tag{3}$$

where λ_1 and λ_2 are both positive regularization parameters.

Anisotropic LSRTM uses anisotropic wavefield modeling operator **L**. We adopt the decoupled P-wave equations in the time-wavenumber domain for 2D TTI media proposed by Zhan et al. (2012):

$$\frac{1}{V_{P_0}^2}\frac{\partial^2 P}{\partial t^2} = -\left\{\begin{array}{l} k_x^2 + k_z^2 \\[6pt] +(2\varepsilon\cos^4\theta + 2\delta\sin^2\theta\cos^2\theta)\dfrac{k_x^4}{k_x^2+k_z^2} + (2\varepsilon\sin^4\theta + 2\delta\sin^2\theta\cos^2\theta)\dfrac{k_z^4}{k_x^2+k_z^2} \\[10pt] +(-4\varepsilon\sin2\theta\cos^2\theta + \delta\sin4\theta)\dfrac{k_x^3k_z}{k_x^2+k_z^2} + (3\varepsilon\sin^2 2\theta - \delta\sin^2 2\theta + 2\delta\cos^2 2\theta)\dfrac{k_x^2k_z^2}{k_x^2+k_z^2} \end{array}\right\}P,\tag{4}$$

where V_{P_0} is the vertical isotropic P velocity; k_x and k_z are the spatial wavenumbers in the x and z directions, respectively; ε, δ and θ are the Thomsen parameters (Thomsen, 1986), where ε describes the difference between the horizontal and vertical P wave velocities (long offset effect), δ is responsible for near-vertical P-wave velocity variations (short offset effect), and θ is the dip angle of the anisotropic symmetry axis.

Our anisotropic LSRTM employs an implicit wavefield-separation scheme. This wavefield decomposition can be made fully automatic and computationally efficient, following a de-primary RTM technology proposed by Fei et al. (2015). The directional components are obtained by

$$I_{\mathrm{pp,down}}(\mathbf{x}) = \sum_{N_s,N_r}\int_0^T [P_sP_r - H_z(P_s)H_z(P_r) - P_sH_z(H_t(P_r)) - H_z(P_s)H_t(P_r)]\,dt$$

$$I_{\mathrm{pp,left}}(\mathbf{x}) = \sum_{N_s,N_r}\int_0^T [P_sP_r - H_x(P_s)H_x(P_r) - P_sH_x(H_t(P_r)) - H_x(P_s)H_t(P_r)]\,dt \tag{5}$$

$$I_{\mathrm{pp,right}}(\mathbf{x}) = \sum_{N_s,N_r}\int_0^T [P_sP_r - H_x(P_s)H_x(P_r) - P_sH_x(H_t(P_r)) - H_x(P_s)H_t(P_r)]\,dt$$

where s and r represent the source and receiver, respectively, P is the separated qP-wavefield, H_x, H_z and H_t represent the Hilbert transform in horizontal direction, vertical direction and time domain, respectively.

3. Synthetic Example

We test our anisotropic LSRTM method on a synthetic "typical" basin and range geothermal model. The model contains several geological sedimentary layers and several fault zones. Fault zones are from offset between different geological layers. We assume that wave propagation along the horizontal direction is 10%~20% faster than that along the vertical direction. For simplicity, we assume elliptical anisotropy (e.g., ε equals δ) and θ is inferred from orientation of reflectors/migration images. Therefore, the constructed fault zones behave as tilted transverse isotropic (TTI) media. We generate synthetic surface seismic reflection data using Vp model (Fig. 2a) and the anisotropic parameters. We compare our anisotropic LSRTM (Fig. 2d) against isotropic LSRTM (Fig. 2b) and anisotropic RTM (Fig. 2c). Figure 2b shows incorrect curved reflectors (enclosed in the red rectangle), because the isotropic model is incorrect. Figure 2c displays

migration artifacts typical of RTM images. Such migration artifacts are harmful because they could be mistaken as valid reflectors. The image of our anisotropic LSRTM suffers fewer migration artifacts as compared to Fig. 2b and Fig. 2c., supporting the effectiveness of our anisotropic LSRTM method.
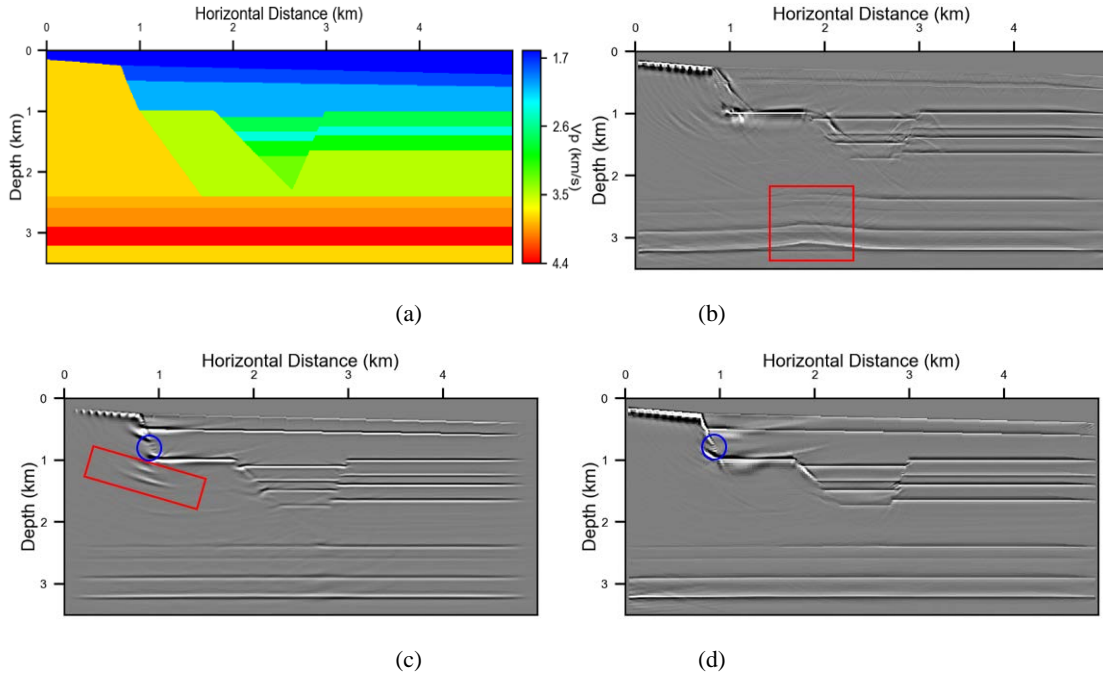
Figure 2: (a) P-velocity model for a "typical" geothermal basin and range where the media is anisotropic. We apply reverse-time migration (RTM) and least-squares reverse-time migration (LSRTM) to produce the following images: (b) Isotropic LSRTM image, (c) Anisotropic RTM image, (d) Anisotropic LSRTM image. Artifacts in (b) and (c) are enclosed in the red rectangles. The gap (in the blue circle) in (c) is wider than the corresponding gap in (d).

4. Anisotropic Least-Squares Reverse-Time Migration of Seismic Data from Eleven-Mile Canyon

We apply anisotropic LSRTM to five 2D lines of surface seismic data acquired at Eleven-Mile Canyon geothermal exploration site in 2013, and compare our results with industrial Kirchhoff migration images and those of anisotropic RTM. For anisotropic RTM and anisotropic LSRTM, we first obtain a velocity model and anisotropic parameters ($V_{P_0}, \varepsilon, \delta, \theta$) using anisotropic full-waveform inversion, starting from an initial velocity model obtained using refraction tomography. To this end, we carry out necessary preprocessing steps, such as converting the phase of the seismic data from 3D to 2D because we perform migration imaging in 2D, and ground-roll noise removal (Huang et al., 2017).

Figures 3–7 show images of the industrial Kirchhoff migration, anisotropic RTM, and anisotropic LSRTM, for seismic survey Lines 1–5. While both anisotropic RTM and anisotropic LSRTM images outperform the industrial images, the case that anisotropic LSRTM outperforms anisotropic RTM is most evidently appreciated regarding Line 4 in Fig. 6. The delineated faults in

our image (Fig. 6c) correspond to those in the lower part of Figure 1, and such faults appear to be clearer than in the anisotropic RTM image (Fig. 6b).

The final data misfit of anisotropic LSRTM reduces to approximately 50-60% of the initial data misfit after 8 iterations. Anisotropic RTM is the first iteration of anisotropic LSRTM. Therefore, our anisotropic LSRTM images are more reliable than those of anisotropic RTM.

(a) Industrial image

(b) Anisotropic reverse-time migration

(c) Anisotropic least-squares reverse-time migration
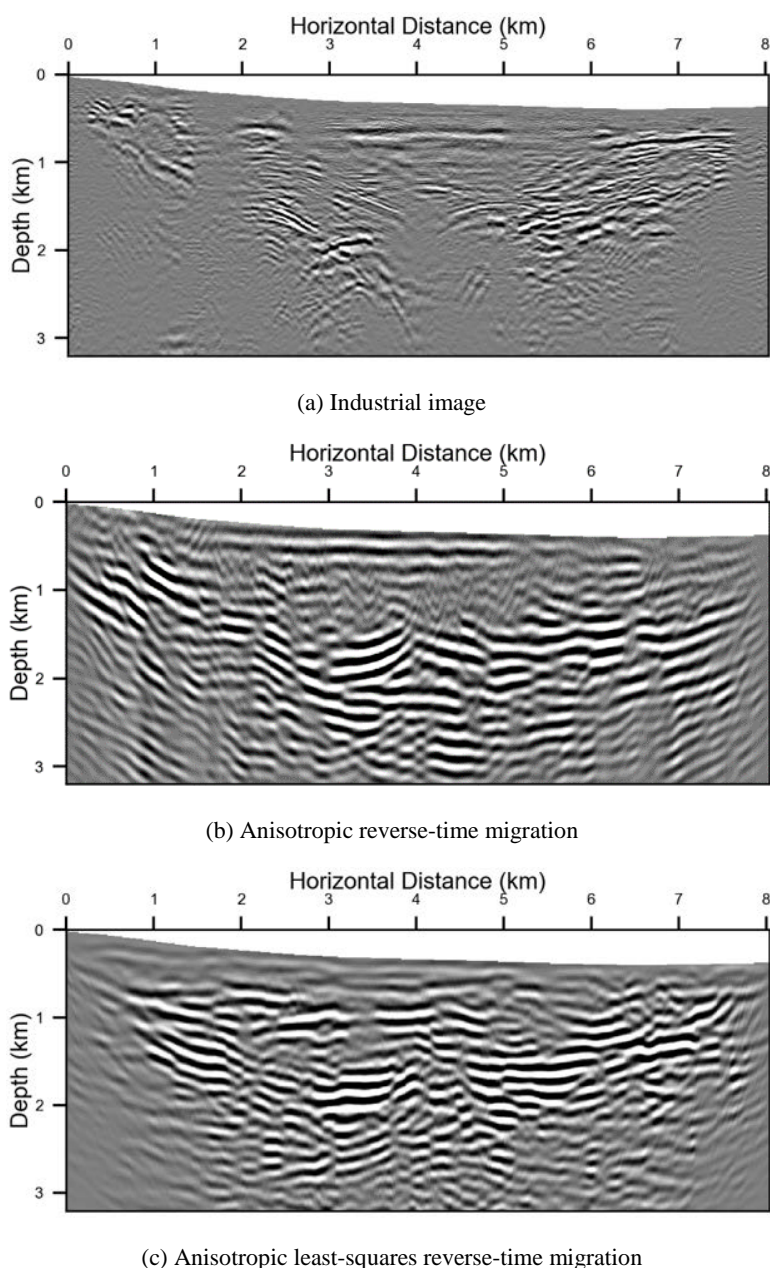
Figure 3: The subsurface migration image of Line 1 computed using various migration methods (a) Industrial Kirchhoff migration image, (b) Anisotropic RTM image, (d) Anisotropic LSRTM image.
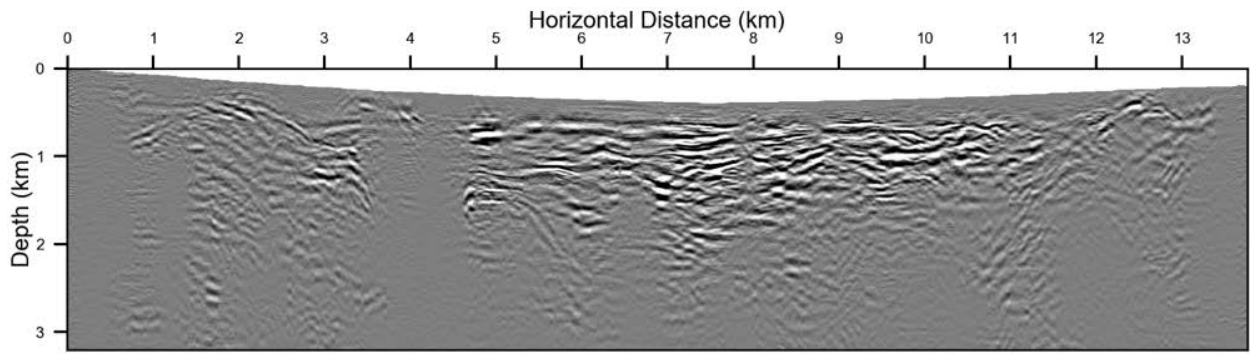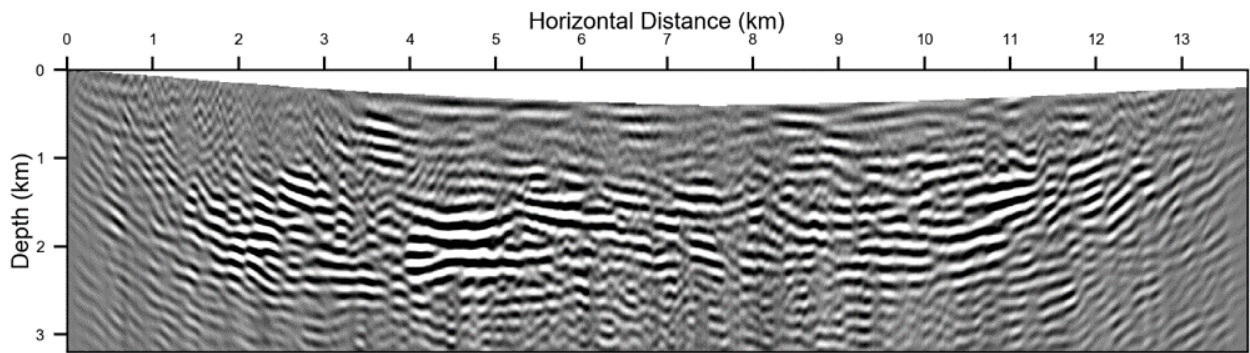
(a) Industrial image

(b) Anisotropic reverse-time migration
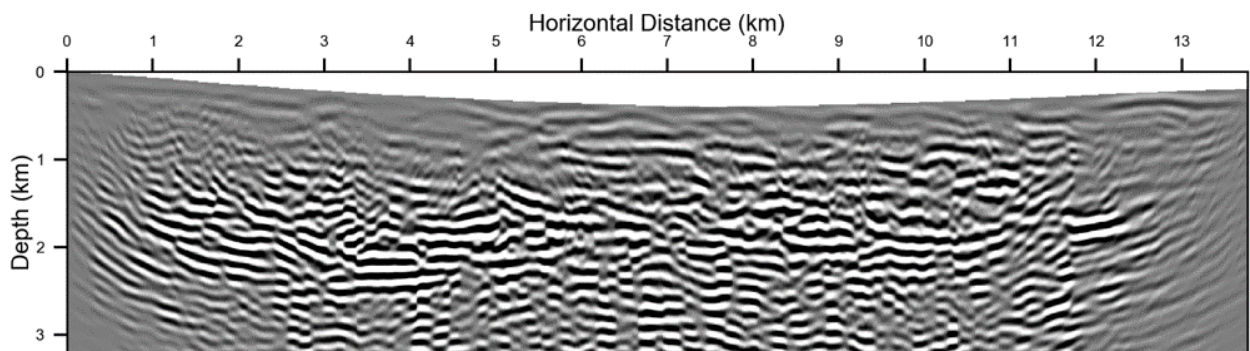
(c) Anisotropic least-squares reverse-time migration

Figure 4: The subsurface migration image of Line 2 computed using various migration methods (a) Industrial Kirchhoff migration image, (b) Anisotropic RTM image, (d) Anisotropic LSRTM image.
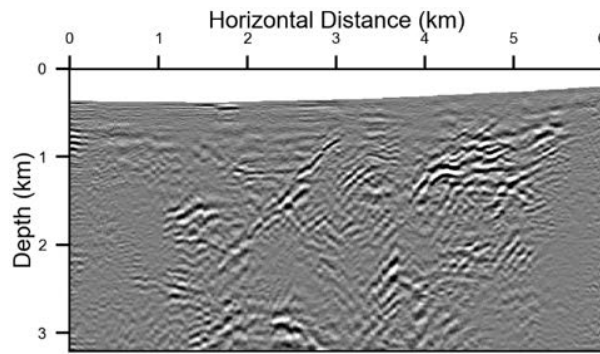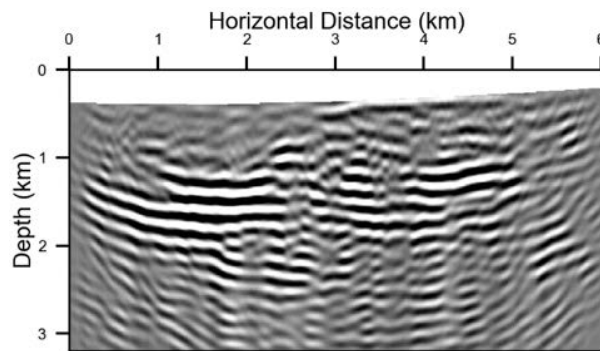
(a) Industrial image

(b) Anisotropic reverse-time migration
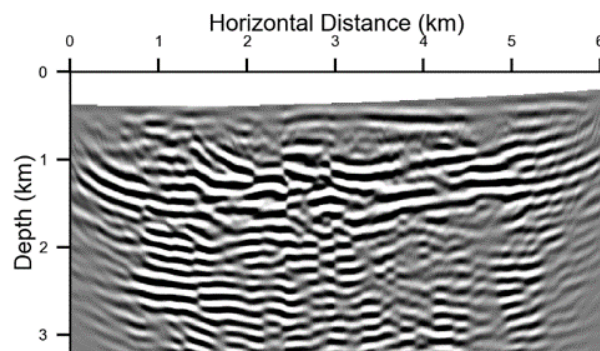
(c) Anisotropic least-squares reverse-time migration

Figure 5: The subsurface migration image of Line 3 computed using various migration methods (a) Industrial Kirchhoff migration image, (b) Anisotropic RTM image, (d) Anisotropic LSRTM image.
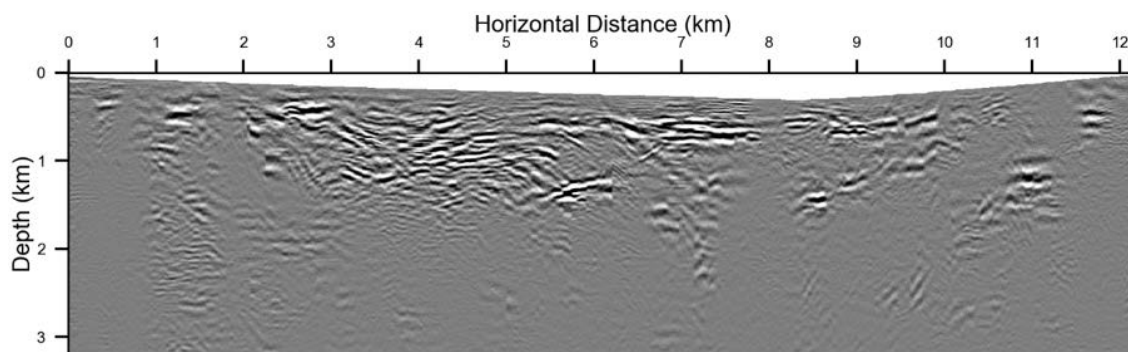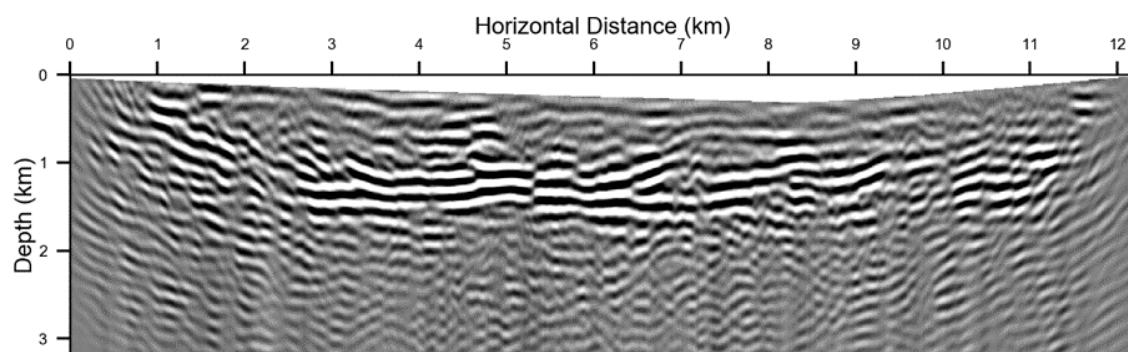
(a) Industrial image

(b) Anisotropic reverse-time migration
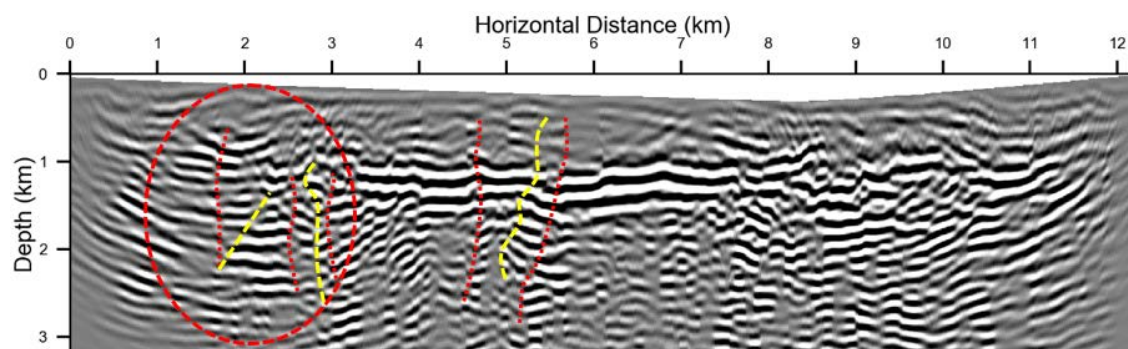
(c) Anisotropic least-squares reverse-time migration

Figure 6: The subsurface migration image of Line 4 computed using various migration methods (a) Industrial Kirchhoff migration image, (b) Anisotropic RTM image, (d) Anisotropic LSRTM image. The delineated faults in (c) correspond to those in the lower part of Figure 1.
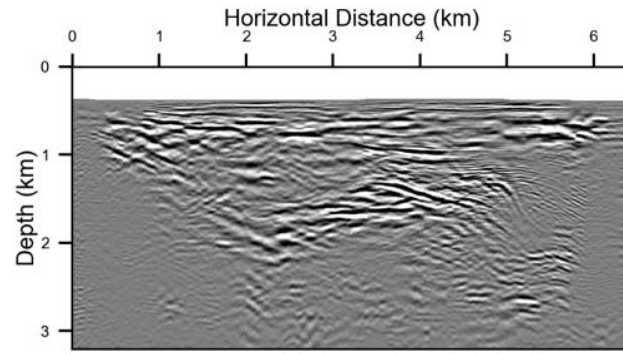
(a) Industrial image
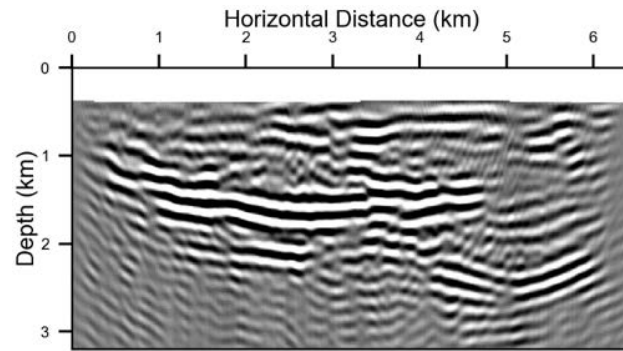
(b) Anisotropic reverse-time migration
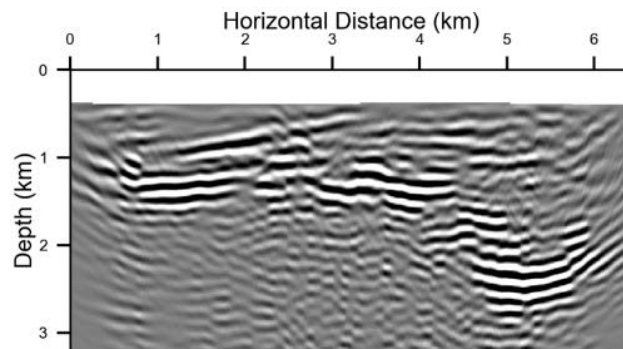
(c) Anisotropic least-squares reverse-time migration

Figure 7: The subsurface migration image of Line 5 computed using various migration methods (a) Industrial Kirchhoff migration image, (b) Anisotropic RTM image, (d) Anisotropic LSRTM image.

5. Conclusions

We have verified the improved imaging capability of our anisotropic least-squares reverse-time migration method using synthetic seismic data for a "typical" basin and range geothermal model. The model contains several fault zones with anisotropic properties. Compared with the two alternative methods of isotropic least-squares reverse-time migration and anisotropic reverse-time migration, our method produces clearer images of fault zones with fewer image artifacts. We have applied our anisotropic least-squares reverse-time migration method to five 2D lines of seismic data acquired at Eleven-Mile Canyon in Nevada. Compared to both industrial Kirchhoff migration and anisotropic reverse-time migration, our method improves the subsurface images significantly,

revealing fracture/fault zones more clearly, some of which are invisible on the other images. This is particularly evidenced by the subsurface images of Line 4, where our image manifests faults consistent with the geology. These results demonstrate that anisotropic least-squares reverse-time migration is an advantageous addition to the state-of-the-art of the anisotropic reverse-time migration for imaging fault/fracture zones for geothermal exploration.

6. Acknowledgments

REFERENCES

Alm, A., Walker, J. D., and Blake, K. "Structural Complexity of the Pirouette Mountain and Elevenmile Canyon Geothermal Systems." *Transactions, Geothermal Resources Council*, 40, (2016), 433-438.

Ba, J., Du, Q., Carcione, J.M., Zhang, H., and Muller, T.M. "Seismic Exploration of Hydrocarbons in Heterogeneous Reservoirs." Elsevier (2015).

Blackwell, D., Waibel, A. F., and Richards. "M. Why Basin and Range Systems are Hard to Find: The Moral of the Story is They Get Smaller with Depth." *Transactions, Geothermal Resources Council*, 36, (2012), 1321-1326.

Caskey, S. J., Wesnousky, S. G., Zhang, P., and Slemmons, D. B. "Surface Faulting of the 1954 Fairview Peak (MS 7.2) and Dixie Valley (MS 6.8) Earthquakes, Central Nevada." *Bulletin of the Seismological Society of America*, 86, (1996), 761-787.

Fei, T., Luo, Y., Yang, J., Liu H., and Qin, F. "Removing False Images in Reverse Time Migration: The Concept of De-primary." *Geophysics*, 80, (2015), S237-S244.

Gao, K., and Huang, L. "Anisotropic Elastic-waveform Modeling for Fracture Characterization in EGS Reservoirs." *Proceedings,* 40th Workshop on Geothermal Reservoir Engineering, Stanford University, Stanford, CA (2015).

Gao, K., Lin, Y., Huang, L., Queen, J., Moore, J., Majer, E. "Anisotropic elastic waveform inversion with modified total-variation regularization." SEG Technical Program Expanded Abstracts (2015), 5158-5163.

Huang, Y., Zhang, M., and Huang, L. "Ground-Roll Noise Suppression in Land Surface Seismic Data Using a Wavenumber-adaptive Bandpass Filter." *Transactions, Geothermal Resources Council*, 41, (2017), 1659-1668.

Nemeth, T., Wu, C., and Schuster, G.T. "Least-Squares Migration of Incomplete Reflection Data." *Geophysics*, 64, (1999), 208-221.

Thomsen, L. "Weak Elastic Anisotropy." *Geophysics*, 51, (1986), 1954-1966.

Unruh, J., Gray, B., Christopherson, K., Pullammanappallil, S., Alm, S., and Blake, K. "Seismic Reflection and Magnetotelluric Imaging of Southwestern Dixie Valley Basin, Nevada." *Transactions, Geothermal Resources Council*, 40, (2016), 455-461.

Zhan, G., Pestana, R. C., and Stoffa, P. L. "Decoupled Equations for Reverse-Time Migration in Tilted Transversely Isotropic Media." *Geophysics*, 77, (2012), T37-T45.

Zhang, M, Kai, G., Huang, Y., Sabin, A., Huang, L. " Imaging Fracture/Fault Zones at Eleven-Mile Canyon in Nevada for Geothermal Exploration Using Anisotropic Reverse-Time Migration." *PROCEEDINGS, 43rd Workshop on Geothermal Reservoir Engineering*, Stanford University, Stanford, CA (2018).